Precision In-Plane Hand Assembly of Bulk-Microfabricated Components for High-Voltage MEMS Arrays Applications

Blaise Gassend, Luis Fernando Velásquez-García, and Akintunde Ibitayo Akinwande, *Fellow, IEEE*

***Abstract*—This paper reports the design and experimental validation of an in-plane assembly method for centimeter-scale bulk-microfabricated components. The method uses mesoscaled deep-reactive-ion-etching (DRIE)-patterned cantilevers that deflect and lock into small v-shaped notches as a result of the hand-exerted rotation between the two components of the assembly. The assembly method is intended for MEMS arrays that necessitate a 3-D electrode structure because of their requirement for low leakage currents and high voltages. The advantages of the assembly method include the ability to decouple the process flow of the components, higher overall device yield, modularity, reassembly capability, and tolerance to differential thermal expansion. Both tapered and untapered cantilevers were studied. Modeling of the cantilever set shows that the springs provide low stiffness while the assembly process is in progress and high stiffness once the assembly is completed, which results in a robust assembly. In addition, analysis of the linearly tapered cantilever predicts that the optimal linearly tapered beam has a cantilever tip height equal to 37% of the cantilever base height, which results in more than a threefold increase in the clamping force for a given cantilever length and deflection, compared to the untapered case. The linear taper profile achieves 80% of the optimal nonlinear taper profile, which would be impractical to fabricate. Analysis of the experimental data reveals a biaxial assembly precision of 6.2-μm rms and a standard deviation of 0.6 μm for assembly repeatability. Electrical insulation was investigated using both thin-film coatings and insulating substrates. Leakage currents less than 1 nA at 2 kV were demonstrated. Finally, this paper provides selected experimental data of a gated MEMS electrospray array as an example of the application of the assembly method. [2008-0113]**

***Index Terms*—Electrospray, high-voltage MEMS packaging, MEMS hand assembly.**

I. INTRODUCTION

In MEMS, it is not uncommon to find centimeter-scale devices having functional elements at the micrometer level. For example, multiplexed MEMS implementations can reach global dimensions that are orders of magnitude larger than the size of their constitutive elements—analogous to very large scale integration (VLSI) chips. In addition, MEMS are typically fabricated using a single substrate and a series of selective deposition and removal of layers of material, where a planar template is directly involved via a lithographic process [1]. However, for some applications, the single-substrate and film processing approach might not be adequate. In particular, there are multiplexed MEMS such as ion, electron, electrospray, and electrospinning sources that are composed of arrays of elements that require high electric fields to operate. The implementation of a proximal annular gate structure surrounding each element substantially decreases the operational voltage of the array. However, even when a microsized gate is employed, the required voltages are still large—sometimes up to several kilovolts. Also, in order to reduce the leakage currents, the physical contact between the electrode and the substrate should be minimized and placed far away from the area where the high electric fields are present. In this case, the aperture in the electrode is effectively hovering in front of each element. The requirements on electrical insulation, operational voltage, and 3-D structure imply that the multiplexed MEMS cannot be easily fabricated using a single substrate and film processing. In more detail, the following examples are discussed.

1) Large arrays of field ionizers require porous structures that increase the neutral particle flux from all directions to the high-field region near the ionizing tip. In order to provide a high-electric-field region with low voltages, a proximal gate that does not restrict the neutral particle flux is required. A gate structure with annular apertures that effectively hovers above the tips would simplify the device fabrication while satisfying these requirements [2].
2) Uniform high-current electron sources can be implemented using large and dense arrays of field emitters that are individually ballasted with a high aspect-ratio, single-crystal silicon column that acts as a current source [3]. Typical gate implementations for field emitter arrays (FEAs) use deposition of dielectric films and planarization of the substrate [4]. However, the aspect-ratio and dimensions of the Si columns could make these steps difficult because of the high stresses from the very thick dielectric films that would be required. Therefore, a gate structure that does not require thick dielectric depositions and substrate planarization, while still being able to provide high fields to the FEAs with low leakage currents, would substantially simplify the device fabrication.

Manuscript received May 5, 2008; revised August 27, 2008. First published February 3, 2009; current version published April 1, 2009. This work was supported in part by the Air Force Office of Scientific Research (with Mitat Birkan as the contract monitor) and in part by Space and Naval Warfare Systems Center Award N66001-04-1-8925 (with Richard Nguyen as the manager). The work of B. Gassend was supported by Prof. Srinivas Devadas (EECS, MIT). Subject Editor L. Spangler.

B. Gassend was with the Massachusetts Institute of Technology, Cambridge, MA 02139 USA. He is now with Exponent, Inc., Menlo Park, CA 94025 USA (e-mail: gassend@alum.mit.edu).

L. F. Velásquez-García and A. I. Akinwande are with the Massachusetts Institute of Technology, Cambridge, MA 02139 USA (e-mail: Velasquez@alum.mit.edu).

Digital Object Identifier 10.1109/JMEMS.2008.2011115

3) Both electrospray and electrospinning sources ionize liquids using high electrostatic fields that transform the meniscus of the liquid into a Taylor cone [5]. The throughput of electrospray/electrospinning sources is significantly increased if large arrays of emitters are operated in parallel [6]–[8]. In an electrospray/electrospinning source, the physical contact between the electrode and the emitter substrate should be minimized to reduce the leakage currents because the per-emitter currents are very small [9], [10]. Also, the physical contact between the electrode and the substrate should occur far from the emitters to decrease the possibility of electrical breakdown due to gate interception or liquid flooding from the start-up transients [11]. A multiplexed electrospray/electrospinning source with an electrode structure that effectively hovers above the emitters would have a simpler fabrication process flow and still be able to provide high fields at the emitters with low leakage currents.

The authors of this paper previously proposed an assembly method for MEMS components that uses deep-reactive-ion-etching (DRIE)-patterned mesoscaled deflection springs, and they reported as an example an out-of-plane component assembly used in a linear array of gated electrospray emitters [6], [12]. The proposed assembly method relies on the tight dimensional control of DRIE parts to achieve MEMS-level assembly precision. The approach of using springs to assemble components is common in macroscale plastic goods [13], although without the same precision and repeatability that were reported. The dimensions of the springs and the forces exerted by them are such that it is feasible to hand assemble the MEMS components. Other benefits of the assembly method are component process flow decoupling, optimization of each component substrate, modularity, larger overall device yield, and the ability to fabricate 3-D devices with out-of-plane dimensions well beyond what is achievable with thin-film processing. The work reported in this paper revisits the proposed assembly method and investigates its use for in-plane assemblies in high-voltage MEMS applications, thus substantially extending the range of devices that could be implemented. The work reported in this paper addresses the questions of alignment precision, assembly repeatability, and electrical insulation for the in-plane case, as well as presents selected experimental data from a gated planar array of MEMS electrospray emitters as an application example. The planar implementation of the assembly method also introduces several improvements over the original report. First, the use of v-shaped notches to lock the spring tips prevents accidental disassembly and provides a reliable way to secure the assembly. Second, the spatial distribution of the springs provides high axial stiffness to tightly control the alignment of the assembly, but the lateral stiffness of the springs is small enough to accommodate differential thermal expansion between the two parts, or consistent over-/underetching of the sidewalls of the components during fabrication. Third, this paper explores the idea of using linearly tapered springs as a way to achieve stiffer springs that require less spring tip displacement to produce the same force.

The in-plane assembly method joins two parts: a disc-shaped object, i.e., twisting component, and a part that has a set of cantilever springs azimuthally distributed, i.e., main body. The assembler of the device first roughly positions the twisting component into a recess on the top surface of the main body, using as guides four protrusions of the main body recess [Fig. 1(a)]. Then, the twisting component is rotated with respect to the main body (clockwise in Fig. 1). As the twisting component rotates, the shape of main body recess forces the center of the twisting component to align within 50 μm of the center of the main body [Fig. 1(b)]. Further movement between the two parts starts to deflect the springs. Finally, each spring tip falls into a notch etched on the edge of the twisting component, thus preventing further rotation and locking the assembly [Fig. 1(c)]. A cross-section of the assembled pair is provided for clarity [Fig. 1(d)]. As guidance, the twisting component has a 24-mm diameter.

The idea of using micromachined springs to interface MEMS systems is not new. They have been used for surface-micromachined components to build 3-D structures from planar components [14], [15], but with components smaller than a millimeter, whereas the work reported in this paper uses centimeter-scale components. Planar snap fasteners have also been made [16], but they are also at a much smaller scale, and allow some wiggle between parts once they have been assembled. The classic micromechanical Velcro [17] shows how to fabricate microhooks on silicon surfaces that mate in a way similar to Velcro. The original micromechanical Velcro did not include positioning, but the formation of mating features that force the silicon parts to assemble in a specific location can also be included [18]. Unlike conventional Velcro, the microfabricated version cannot be disassembled without destroying the microhooks. Snap systems have also been used to attach optical fibers to substrates [19].

The choice of using an in-plane spring assembly could be perceived as unnecessary because of the availability of several wafer-bonding techniques. The authors of this paper believe that spring-based methods are superior to other wafer-bonding methods to integrate electrode systems to high-voltage MEMS arrays for a number of reasons. First, the assembly is not permanent and can be remade multiple times. Therefore, iteration of the twisting component design can be carried out using the same main body, and *vice versa*. Moreover, modular designs that swap electrode systems for different applications of the same emitting array can also be implemented. Second, spring-based assemblies give more freedom in the choice of substrates to be bonded, thus providing more flexibility to the design. Third, the assembly does not require high pressure or high temperature. Therefore, the assembly method does not impact the thermal budget of the device and also allows the use of temperature-degradable films and substrates such as polymer-based materials. Nevertheless, the assembly method is compatible with high-temperature processing. Fourth, the hand assembly step requires no special equipment, which improves manufacturing flexibility, at least at the research and development level.

A test structure was microfabricated to investigate the precision, repeatability, and electrical insulation capabilities of the in-plane assembly method. Fig. 2 shows a completed test structure and a close-up view of the springs activated, with their tips clamped into the notches of the twisting component.

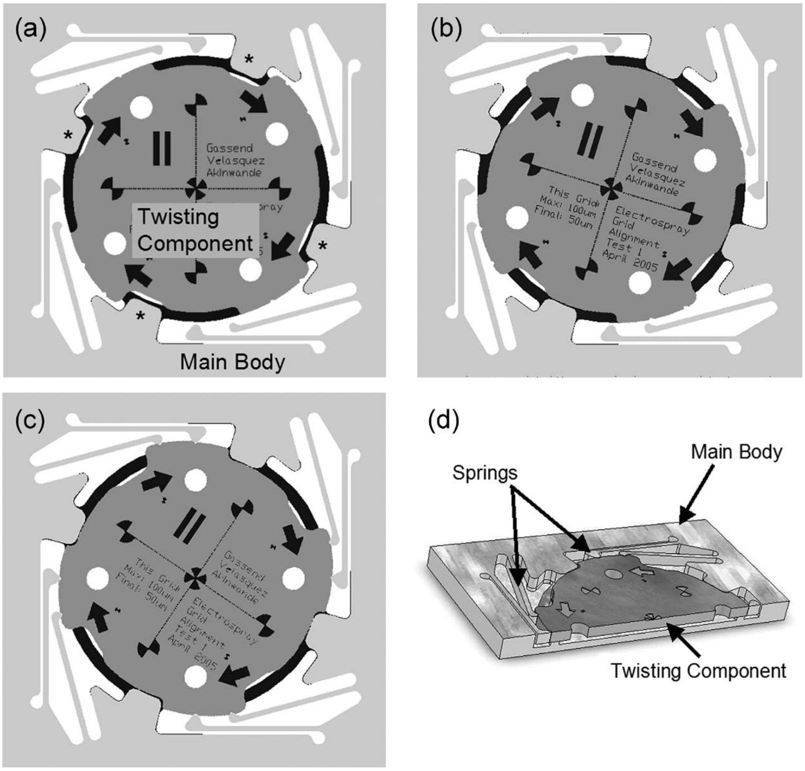

Fig. 1. In-plane hand assembly of the twisting component and the main body. (a) First, the twisting component is placed inside the recess of the main body, using as guides four protrusions or twisting component stops, denoted by "∗." (b) Then, the rotation of the twisting component with respect to the main body forces the twisting component into rough alignment. Continued rotation of the twisting component causes the springs to deflect. (c) Finally, the spring tips clamp into notches etched in the twisting component, locking the assembly. (d) A 3-D view of the assembly is shown for clarity.

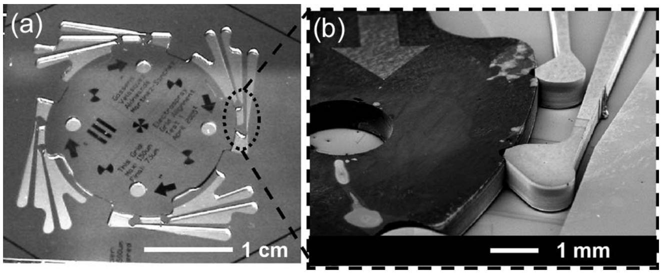

Fig. 2. (a) Completed test structure and (b) a close-up view of a spring cluster of an assembled test structure. Four spring clusters, with each cluster being composed of two springs, are uniformly and azimuthally distributed around the twisting component to provide low stiffness while the assembly is in progress and high stiffness once the assembly is completed.

The test structure includes sets of crosshairs for conducting metrology on the assembly. The test structure was fabricated using DRIE and fusion bonding. It requires the bonding of two wafers to create the main body. Fusion bonding was selected because, in the experience of the authors, such bonding technique introduces very little misalignment, which would substantially simplify the benchmarking of the in-plane spring assembly. Of course, the assembly method can also be implemented on devices with low-temperature processing requirements. In Section II, the design of the test structure is described. In Section III, the fabrication process of the test structure is reported. Finally, Section IV covers the metrology and electrical characterization of the assembly method and provides selected data of a planar array of electrospray emitters as an application example of the in-plane assembly method.

II. TEST STRUCTURE DESIGN AND MODELING

This section addresses the design, robustness, and expected mechanical performance of the in-plane assembly method. The design of the in-plane assembly intends to provide stiff and accurate positioning of the assembled parts while ensuring modularity and flexibility in the choice of component substrates used in the fabrication process flow. In addition, the design intends to achieve a robust assembly, i.e., difficult to break, tolerant to process variation, and easy to implement. In this section, silicon is modeled as an isotropic elastic material, although silicon is a cubic material. It is possible to estimate equivalent isotropic elastic constants for a cubic material by averaging on all directions the orientation-dependent elastic constants [20]. Using the analysis of the cited reference results in an average Young's modulus of 145 GPa, while the orientation-dependent Young's modulus varies from 130 GPa for [100] to 168 GPa for [110] [21], which are within 15% of the average Yong's modulus. Modeling silicon as an isotropic elastic material results in a small difference in the estimates compared to modeling silicon as a cubic elastic material [22].

A. Spring and Notch Design

Cantilever springs were used in the design of the in-plane mechanical assembly. Both constant cross-sectional cantilevers and linearly tapered cantilevers were implemented, as seen in Table I. Each spring tip interacts with the edge of the twisting component. Fig. 3 shows the motion that a spring tip follows

TABLE I
DIE VARIATIONS ON SPRING GEOMETRY, NOMINAL, AND MAXIMUM SPRING TIP DEFLECTIONS

Spring Type	Spring Geometry	Twisting component Type	Maximum/Minimum spring tip deflection (μm)
I	Straight: H = 550 μm	A	100/50
II	Tapered: H_1 = 700 μm, H_2 = 260 μm	B	50/25
III	Tapered: H_1 = 1000 μm, H_2 = 370 μm	C	150/75

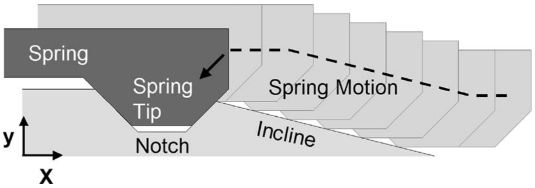

Fig. 3. Motion of a spring tip during assembly. After traveling on the edge of the twisting component, each spring tip falls into a v-shaped notch to lock the assembly.

during assembly of the twisting component with respect to the main body. In this figure, the parts to be mated are translated relative to one another in the x-direction. Initially, the spring tip is free, but then the tip comes into contact with the edge of the twisting component as it rotates. Relative rotation of the two parts causes the spring to slowly deflect due to its interaction with a gentle incline on the edge of the twisting component. Finally, continued rotation causes the spring tip to click into a notch etched on the edge of the twisting component. In the final position, the spring is still deflected, exerting a clamping force on the notch. In the figure, the clamping force is in the y-direction, perpendicular to the direction of relative motion of the two parts while being assembled. This feature in the design prevents the clamping force from creating a systematic shift in the final resting position of the spring tip. Specifically, the spring has low stiffness in the y-direction (the beam is in flexion) and high stiffness in the x-direction (the beam is in tension/compression).

The interface between the spring tip and the notch consists of two inclined planes. The angle of inclination is the same on both sides. Thus, any systematic over- or underetching will change the final deflection of the spring tip, but it will not alter its position in the x-direction relative to the notch. If the interface planes have steep angles, a small x-error translates to a large spring tip deflection, thus creating a large restoring force that tries to center the spring tip in its notch. However, a steep angle at the interfaces also leads to higher sensitivity to process variation because, for a given over- or underetch, a steeper angle corresponds to a larger change in spring tip deflection. An interface angle of 45° was chosen as a compromise between the two effects.

The amount of motion that the spring tip undergoes during assembly is another tradeoff. The maximum spring tip deflection is larger than the final spring tip deflection because of the presence of a notch in the twisting component to lock the assembly. In the design of all the spring types, the maximum spring tip deflection was set at twice the final spring tip deflection. For a given clamping force, the spring length L increases with the maximum allowable spring tip deflection. Therefore, small deflections are recommended in the design. However, the spring tip deflection should be large enough to guarantee a proper assembly, even if process variations occur. The minimum spring tip deflection $\Delta_{\min}$ is

$$\Delta_{\min} = 2\delta + \frac{F_{\min}}{K_B} \tag{1}$$

where δ is the allowed under-/overetching variation on each component of the assembly, K_B is the bending stiffness of the spring, and $F_{\min}$ is the minimum per-spring clamping force. Variations on the maximum (assembly is in progress) and final spring tip deflection were implemented to investigate the influence of the magnitude of the clamping force on the assembly. The final spring tip deflection span the 25–75-μm range (Table I, right-hand side). Therefore, the reported in-plane assembly test structures can tolerate a maximum over-/underetching of at least 12.5 μm on each of the assembled components while still producing a nonzero per-spring clamping force. Variations in the dimensions of the microfabricated components mainly come from photolithography, hard-mask patterning, and DRIE of the substrates. In the experience of the authors, contact photolithography should have a dimensional-variation upper bound on the order of 2–3 μm for a 10-μm-thick photoresist film. Also, in their experience, the hard-mask-etching dimensional-variation upper bound should be on the order of 1–2 μm if thick oxide films (10 μm) are patterned with a reactive ion etching step (80° or steeper sidewalls). The DRIE taper depends on the size of the etching window and the particular etching recipe that is used [12]. Optimization of the DRIE parameters should result to first-order perpendicular sidewalls, as many researchers have demonstrated. If Gauss' law of error propagation is assumed, these three independent effects (lithography variation, hard mask etching variation, and DRIE sidewall taper) produce a combined dimensional variation in the twisting component and the main body on the order of 3.5 μm, which is almost an order of magnitude smaller

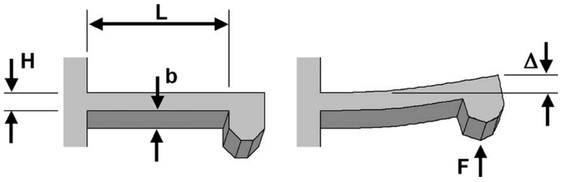

Fig. 4. Schematic of the type-I spring. The spring has length L, width b, and height H. The spring produces a clamping force F when the spring tip is deflected Δ.

than the minimum spring tip deflection value. Other fabrication methods, such as laser cutting, are likely to have larger over-/underetch.

1) Uniform Cross-Sectional Springs: The type-I springs (Table I) are slender cantilevers with uniform cross section (Fig. 4). These springs produce a point force F at their tips when deflected. The type-I springs were designed using the analysis from [12]. The bending stiffness K_B and maximum bending stress $\sigma_{\max}$ for the type-I springs are

$$K_B = \frac{F}{\Delta} = \frac{E \cdot b}{4}\left(\frac{H}{L}\right)^3 \tag{2}$$

$$\sigma_{\max} = \frac{3E \cdot H \cdot \Delta}{2L^2} \tag{3}$$

where E is the Young's modulus of the material, b is the width of the spring, H is the height of the spring (dimension of the spring in the direction of the beam deflection), L is the spring length, and Δ is the spring tip deflection. By eliminating H in (2) and (3), an expression that shows the tradeoff between force, deflection, and spring length can be obtained

$$\frac{F \cdot \Delta^2}{L^3} = \frac{2}{27}\frac{b \cdot \sigma_{\max}^3}{E^2}. \tag{4}$$

The right-hand side of (4) is only determined by the spring substrate. For a 650-μm-thick silicon wafer, $b = 650$ μm and $E = 145$ GPa [20]. Limiting the maximum tensile bending stress to a conservative value of 100 MPa (an order of magnitude smaller than the maximum tensile stress in single-crystal silicon [22]), the right-hand side of (4) is equal to 2.3 mN/m.

The dimensions of the springs used in the in-plane test structure came from design considerations for a planar array of electrospray emitters (see Section IV) and from (4). The interaction between the performance requirements, layout dimensions, and fabrication process of the application resulted in six devices if 6-in Si substrates were used. The number of devices results from using a hexagonal packing to maximize the area utilization of the substrate. The design limited the spring length to about a centimeter. If a maximum spring tip displacement of 100 μm is used, (4) limits the per-emitter clamping force to about 0.25 N, while (2) sets the length-to-height ratio L/H to about 20. The actual dimensions of the type-I springs are $L = 1.09$ cm, $H = 550$ μm, and $b = 650$ μm. These springs produce a clamping force of 0.3 N for a spring tip deflection of 100 μm.

2) Linearly Tapered Springs: Improved tradeoffs are possible for springs based on tapered cantilevers, which are thick near their base and skinny further out where the bending moment is smaller. As in the case of the constant cross-sectional springs, the design of the tapered spring geometry should maximize the allowable spring tip deflection and clamping force while minimizing the spring length to save device footprint. In a tapered cantilever, the beam height H can be described as [23]

$$H(x) = h_o \cdot s\left(\frac{x}{L}\right) \tag{5}$$

where h_o is a characteristic height, L is the cantilever length, s is a function that characterizes the shape of the beam, and x is the distance from the base of the cantilever. A force F applied at the spring tip causes a deflection Δ of the tip that can be computed using the slender beam methods [24]

$$\Delta = 4\frac{F \cdot L^3}{E \cdot b \cdot h_o^3}\int_0^L\int_0^{u_1} 3\frac{1-u}{s(u)^3}du \cdot du_1 = 4\frac{F \cdot L^3}{E \cdot b \cdot h_o^3}f_s \tag{6}$$

where u and u_1 are integration variables, and the shape dependence is lumped into the parameter f_s, which is unity for a cantilever with constant height h_o. Using the same reference, the equation that relates the spring geometry with the maximum allowable stress $\sigma_{\max}$ is

$$\sigma_{\max} \geq 6\frac{F \cdot L}{b \cdot h_o^2}\max_{0 \leq u \leq L}\left(\frac{1-u}{s(u)^2}\right) = 6\frac{F \cdot L}{b \cdot h_o^2}g_s \tag{7}$$

where the shape dependence is lumped into the parameter g_s, which is unity for a cantilever with constant height h_o. Eliminating h_o from (6) and (7) yields the inequality

$$\frac{F \cdot \Delta^2}{L^3} \leq \frac{2}{27}\frac{b \cdot \sigma_{\max}^3}{E^2} \cdot \frac{f_s^2}{g_s^3} = \frac{2}{27}\frac{b \cdot \sigma_{\max}^3}{E^2}S_S \tag{8}$$

where the factor S_S contains the shape dependence. There is a tradeoff between increasing force and deflection and decreasing spring length, analogous to (4). However, optimizing the spring shape can improve the tradeoff by increasing S_S, which is unity for a spring with constant cross section.

The shape of the optimal beam geometry can be found from (7). If $(1-u)/s(u)^2$ is not equal to g_s everywhere, then S_S can be augmented by decreasing $s(u)$ at points where the equality is not satisfied. Indeed, this operation does not change g_s, but causes f_s to increase, resulting in a net increase in S_S. Thus, for the optimal shape, $(1-u)/s(u)^2$ is uniform. In the optimal geometry, the height is proportional to the square root of the distance to the spring tip

$$s(u) = \sqrt{1-u}. \tag{9}$$

This geometry yields $f_s = 2$ and $g_s = 1$, so $S_S = 4$. Therefore, spring tapering can yield a fourfold improvement over the constant cross-sectional spring in (8). However, the optimal spring shape is impractical, as its height is zero at the tip, in which case the shear stress near the tip becomes the dominant failure mechanism. Moreover, the spring tip must be shaped to fit into its notch, which implies a nonzero height at the spring

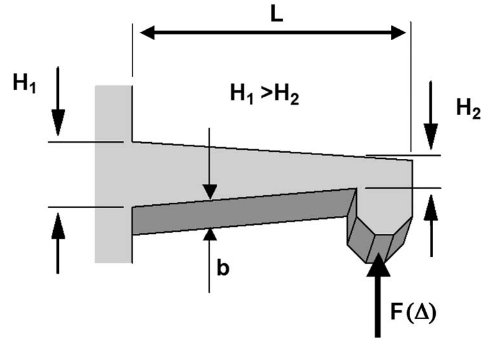

Fig. 5. Schematic of a linearly tapered cantilever (spring types II and III). The spring has length L, width b, base height H_1, and tip height H_2. A force F is produced at the spring tip due to the tip deflection Δ.

tip. These difficulties could be solved by using the optimal spring shape far from the spring tip and then transitioning to a constant height spring near its tip. However, a linearly tapered spring (Fig. 5) can achieve an S_S factor close to the optimal case. A linearly tapered spring has a shape s_γ

$$s_\gamma(u) = 1 + \gamma \cdot u \tag{10}$$

where $\gamma > -1$ determines the decrease in height from the spring base, i.e., H_1, to the spring tip, i.e., H_2. In other words,

$$h(x) = H_1 \left(1 + \frac{H_2 - H_1}{H_1} \frac{x}{L}\right). \tag{11}$$

Using (6) and (7), for a linearly tapered spring, the shape factors f_s and g_s are

$$f_s = \frac{3}{\gamma^3}\left[\ln(1+\gamma) + \frac{\gamma^2}{2} - \gamma\right] \tag{12}$$

$$g_s = \begin{cases} 1, & \gamma \geq -\frac{1}{2} \\ -\frac{1}{4\gamma(\gamma+1)}, & -1 \leq \gamma \leq -\frac{1}{2}. \end{cases} \tag{13}$$

Numerically, the optimal linear taper occurs when $\gamma = -0.63$, i.e., the spring height at its tip is 37% of the spring height at its base. For this slope value, S_S is equal to 3.21, i.e., 80% of the theoretical limit (Fig. 6). Two kinds of linearly tapered springs with $\gamma = -0.63$ were implemented in the in-plane assembly test structures (Table I). The type-II spring is a tapered spring with $H_1 = 700$ μm and $H_2 = 260$ μm. The type-III spring is a tapered spring with $H_1 = 1000$ μm and $H_2 = 370$ μm. The type-II spring is 5% stiffer than the type-I spring. The type-III spring is nearly three times stiffer than the type-I spring, thus producing a clamping force of about 0.68 N if the spring tip is deflected by 75 μm.

3) Disassembly-Force Failure Modes: In [12], the authors proposed a nominal per-spring clamping force of about 1 N. Therefore, frictional forces on the order of a fraction of a newton would occur while the assembly process is in progress. The magnitude of the frictional force during assembly should be discernable (tactile sensing) from the reaction force experienced when the assembly process is completed (locked). The reaction force after spring locking is given by the interaction between the spring tip and the notch (Fig. 7). Since the notch is symmetric, for either sense of rotation, it can readily be shown that the minimum per-spring disassembly force F_D is

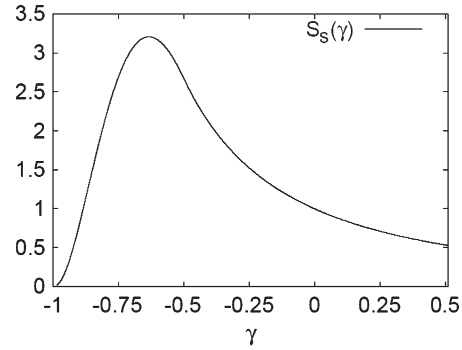

Fig. 6. S_S versus γ for a linearly tapered cantilever. S_S is the shape factor that lumps the functional dependence of the spring tip deflection (denoted by the function f_s) and maximum bending stress (denoted by the function g_s) on the geometry of the cantilever. The fractional change in beam height across the length of the cantilever, i.e., $(H_2 - H_1)/H_1$, is denoted by γ. S_S reaches a maximum value of 3.21 at $\gamma = -0.63$, i.e., when the cantilever height at the tip is 37% of the cantilever height at the base.

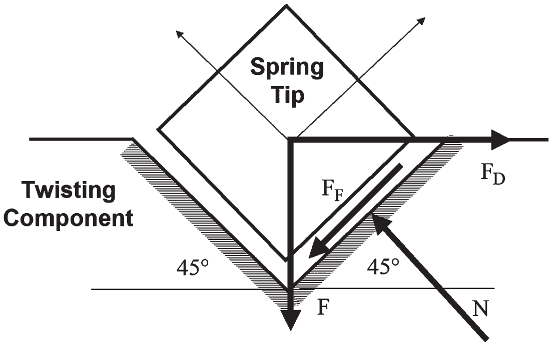

Fig. 7. Simplified force diagram of the twisting component if rotated to cause disassembly. The spring clamping force F and the disassembly force F_D generate a reaction normal force N from the notch. The normal force produces a static frictional force F_F at the spring tip/notch interface. The frictional force and the clamping force counteract the disassembly force until the disassembly force reaches a threshold value given by (14).

$$F_D = \frac{\tan(\theta) + \mu_S}{1 - \mu_S \cdot \tan(\theta)} F \tag{14}$$

where F is the clamping force, θ is the inclination angle of the notch (45°), and μ_S is the static friction coefficient, which is about 0.3 for DRIE sidewalls [25]. Therefore, a force of about 1.86 times the clamping force is needed for disassembly. For an n-spring system, the hand would need to apply a torque such that it produces a force F_D on each spring, i.e., a total force F_H

$$F_H = n \cdot F_D. \tag{15}$$

For the eight-spring system, the force is equal to 8 F_D, or a total force on the order of 15 N. This force is at least an order of magnitude smaller than the maximum force that the springs can withstand if placed in tension $F_{T,\max}$

$$F_{T,\max} = \sigma_{\max} \cdot b \cdot H \tag{16}$$

equal to 169 N for the type-II springs—which have the smallest cross section of the set. The force predicted by (15) is also

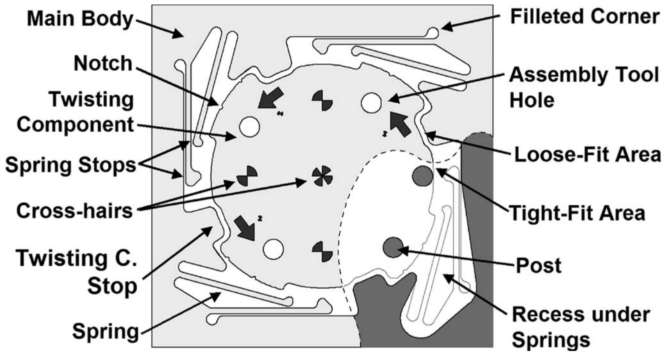

Fig. 8. Detailed schematic of the in-plane assembly test structure.

substantially smaller than the force required for buckling. The buckling model that most closely matches the real situation is a column that has one end fully constrained, and the other has restrictions on the displacement in the direction of the deflection due to bending. For a spring with constant cross section, the maximum force F_p before buckling is [23]

$$F_P = \frac{\pi^2}{6} E \frac{b \cdot H^3}{L^2}. \tag{17}$$

Therefore, the buckling force of the type-I spring is 217 N. For the type-II and type-III springs, the buckling force is larger than what is predicted by (17) because these springs are stiffer than the type-I spring. For the type-II spring, the buckling force would be larger than the maximum compressible force due to maximum stress [also (16)], so this latter limit would occur first. The values of the assembly frictional force and the maximum reaction force before disassembly are in agreement with recent research results on the field of human–machine interfaces. In particular, it has been determined that the human hand can resolve a force as small as 0.1 N [26], [27]. The friction force of the eight-spring system is above this value, so the brain will be able to discern that the assembly is in progress. It has also been shown that hand-actuated interfaces should produce a reaction force of at least 1.5 N in order to be discernable by most users that the actuation has been achieved [26]. The maximum reaction forces before disassembly can be at least two orders of magnitude above this value. Therefore, they should be large enough for the brain to discern that the assembly process is completed.

B. Assembly Robustness

The robustness of the assembly comes from the properties of the springs and the spatial distribution of the spring set. The twisting component is assembled to the main body by producing a relative rotation between the two parts, and the springs are grouped in four pairs that are evenly distributed around the twisting component (Fig. 8). This spatial distribution produces several benefits. First, if there are three or more springs with their spring tips in their corresponding notches, the stiffness of the assembly will be determined by the axial stiffness of the springs, as opposed to the much lower flexural stiffness that dominates the assembly process. Second, only the spring tips hold the twisting component. Therefore, any systematic over-/underetching or any differential thermal expansion would only cause the assembly components to be slightly larger or smaller than expected. The change in size of the assembly components can be accommodated by spring deflection with no first-order error in the assembly alignment. Third, when the assembly is complete, each spring pair exerts a force with a line of action that passes through the center of mass of the twisting component [see, for example, Fig. 1(c)]. Therefore, each spring pair exerts to first-order zero torque to the assembly.

The design includes a series of features to protect the springs from accidental damage due to excessive deflection (Fig. 8). First, the springs are etched into the main body, where they are better sheltered than on the periphery of the twisting component. Second, the twisting component is inserted using as guides four protrusions or twisting component stops. These features limit the movement of the twisting component, so it can be wiggled around without exerting excessive deflection to the springs. The twisting component stops also prevent the twisting component from being counter rotated. Third, as the twisting component is rotated into place, the gap between the border of the twisting component and the twisting component stops sets the maximum wiggle to 50 μm, thus restricting the deflection of the springs below their deflection breaking value. Fourth, there are spring stops that prevent the springs from excessively deflecting outward. Fifth, the geometry of the assembly components is smooth to avoid stress concentrators. Sixth, the assembly has a total of eight springs to provide some redundancy in case some of the springs are lost. More springs could be included, but they would occupy valuable surface area. Also, while conducting experiments with a 36-device set, most devices did not lose any springs, and no more than two springs were lost in a single device. However, it was possible to assemble the twisting component to the main substrate with the same precision in the devices that lost springs.

C. Expected Performance

The following analysis demonstrates that the in-plane assembly method provides high stiffness to the assembly. Consider that the twisting component undergoes a small translation (t_x, t_y), and assume that the spring tips remain in their notches without buckling or snapping. Also, suppose that the joints are frictionless and unable to transmit any moments. Therefore, the forces $F_{x,i}$ and $F_{y,i}$ that are exerted by a spring with an axis along the x-direction are determined by the axial stiffness K_A and bending stiffness K_B

$$\begin{pmatrix} F_{x,i} \\ F_{y,i} \end{pmatrix} = -\begin{pmatrix} K_A & 0 \\ 0 & K_B \end{pmatrix} \begin{pmatrix} t_x \\ t_y \end{pmatrix} \tag{18}$$

where K_A and K_B are defined for a spring with constant cross-section as

$$K_A = \frac{E \cdot b \cdot H}{L} \tag{19}$$

$$\frac{K_A}{K_B} = 4 \left(\frac{L}{H} \right)^2 \gg 1 \tag{20}$$

TABLE II
TYPES OF TWISTING-COMPONENT-TO-MAIN BODY SURFACE INTERFACE IMPLEMENTED IN THE DIE SET

Interface Type	Twisting component-to-Main Body Interface Surface Type
P	A set of 8 circular posts disposed on a circle
R	A continuous ring.

and, for the case of a linearly tapered spring, as

$$K_A = \frac{E\cdot b\cdot H_1}{L}\frac{\gamma}{\ln[\gamma+1]} \tag{21}$$

$$\frac{K_A}{K_B} = 4\frac{\gamma\cdot f_s}{\ln[1+\gamma]}\left(\frac{L}{H_1}\right)^2 \gg 1. \tag{22}$$

For a set of n springs evenly distributed around the device, the total force is then [28]

$$\begin{pmatrix}F_X\\F_y\end{pmatrix} = -\sum_{i=0}^{n-1}\begin{pmatrix}\cos(2\pi\cdot i/n) & \sin(2\pi\cdot i/n)\\ -\sin(2\pi\cdot i/n) & \cos(2\pi\cdot i/n)\end{pmatrix}\begin{pmatrix}K_A & 0\\ 0 & K_B\end{pmatrix} \times\begin{pmatrix}\cos(2\pi\cdot i/n) & \sin(2\pi\cdot i/n)\\ -\sin(2\pi\cdot i/n) & \cos(2\pi\cdot i/n)\end{pmatrix}\begin{pmatrix}t_x\\t_y\end{pmatrix}. \tag{23}$$

If $n > 3$, the sum simplifies to an isotropic stiffness of

$$K = \frac{n}{2}(K_A + K_B) \cong \frac{n}{2}K_A. \tag{24}$$

If the springs are not evenly spaced around the twisting component, but can be partitioned into groups of springs that are uniformly distributed, then this result still applies. From (19)–(22), the equivalent spring stiffness is then

$$K = \frac{n}{2}\frac{E\cdot b\cdot H}{L} \tag{25}$$

for the constant cross-sectional spring case and is

$$K = \frac{n}{2}\frac{E\cdot b\cdot H_1}{L}\frac{\gamma}{\ln[\gamma+1]} \tag{26}$$

for the linearly tapered spring case. For the eight-spring assembly, the values of K are 19 N/μm for the type-I spring, 15.4 N/μm for the type-II spring, and 21.9 N/μm for the type-III spring. Therefore, at least 385 N is needed to produce a displacement that is larger than any of the nominal spring tip deflections (the spring tip is released from the notch). The stiffness of the springs also gives the assembly robustness to inertial forces because the mass of the twisting component is only about 0.5 g. For example, a twisting component type A (Table I) held by type-I springs receives a total clamping force of 1.2 N if each spring tip is deflected 50 μm while locked into its corresponding notch (each spring exerts a force equal to 0.15 N). Hence, the maximum static friction force before sliding is 0.36 N if a static friction coefficient equal to 0.3 is assumed [25]. Therefore, the twisting component can resist out-of-plane accelerations as large as 72 g before it detaches from the main body. Similarly, the rotational stiffness K_θ is

$$K_\theta = 2r^2\cdot K \tag{27}$$

where r is the distance from the center of the twisting component to the spring tip (about 1.2 cm). In (25) and (26), the factor 1/2 comes from the observation that, in a linear displacement, half the springs of the n-set are activated. In (27), the factor 2 comes from the observation that, in a rotation, all the fingers are identically loaded along their axial direction, i.e., all the springs of the n-set are activated.

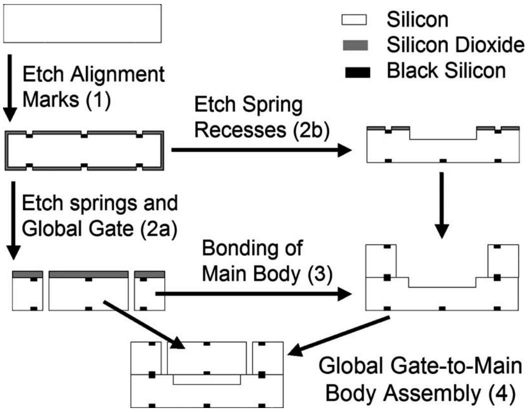

Fig. 9. Fabrication process flow. Process flow for the top wafer: (1) Etching of metrology features and (2a) DRIE of the twisting component and spring sets. Process flow bottom wafer: (1) Etching of metrology features and (2b) etching of spring recesses. Final processing: (3) Bonding of the main body and (4) assembly of the twisting component to the main body.

D. Exploration of the Dependence of the Assembly Alignment on the Main Body Topography

Finally, variations on the surface of the main body that is right below the twisting component were implemented (Table II) to study the dependence of the assembly repeatability on the topography of such surface. One surface (interface of type P) was composed of eight small circular posts that were 100 μm tall and 2 mm wide, evenly spaced along a circle with radius equal to 1 cm. The other surface (interface of type R) had a continuous ring that was 100 μm tall with inner radius equal to 1.09 cm and outer radius equal to 1.19 cm. The R-type interface has almost three times the surface right below the twisting component of the P-type interface.

III. FABRICATION

The fabrication of the devices took place at the MIT Microsystems Technology Laboratories (MTL). Fig. 9 shows a schematic of the fabrication process flow. The process flow uses two 650-μm-thick double-side-polished 6-in silicon wafers and three contact masks. First, a silicon dioxide film that is 0.3 μm thick is grown on the wafers to protect the bonding surfaces from damage during processing. Then, a set of crosshairs for metrology on the assembly is etched on both sides of the wafers by conducting contact photolithography on a 1-μm-thick spun photoresist, followed by a BOE bath to etch the exposed oxide and a shallow plasma etch of the exposed silicon surface [Fig. 9(1)]. The plasma produces black silicon [29], which increases the contrast of the crosshairs. The two wafers are cleaned using a piranha bath. After that, both wafers receive a 5-μm-thick plasma-enhanced chemical-vapor-deposited (PECVD) silicon oxide film on one of the surfaces. The wafers are annealed in nitrogen at 950 °C. The film will be used as hard mask in later processing steps. Next, the features of the springs and twisting component are defined on the top wafer by conducting contact photolithography on a spun photoresist film that is 10 μm thick. The twisting components fit in the empty space surrounded by the spring sets, thus allowing the two features to be combined in the same mask and use the same substrate. The exposed oxide film is etched using an Ar/CHF_3/CF_4 plasma, and then, the wafer is mounted to a quartz handler wafer using photoresist. The top wafer is etched through with a DRIE step [Fig. 9(2a)]. The top wafer is dismounted using acetone, and then, the top wafer and twisting components are cleaned using a piranha bath followed by oxygen plasma. Subsequently, the spring recesses are defined on the bottom wafer by conducting contact photolithography on a spun photoresist film that is 10 μm thick. The exposed oxide film is etched using an Ar/CHF_3/CF_4 plasma, and then, the exposed silicon is etched with a DRIE step to a depth of 100 μm [Fig. 9(2b)]. The recesses avoid bonding of the springs to the bottom substrate and allow the springs to deflect without interacting with the bottom wafer. The bottom wafer is cleaned in a piranha bath followed by an oxygen plasma treatment. Once the etching is completed, the oxide on both wafers is stripped using a 50% HF dip. This is followed by an RCA clean (HF dip is skipped) and fusion bond at 1050 °C to make the main body of the in-plane assembly test structure [Fig. 9(3)]. Afterward, the wafer stack is die sawed. Finally, the twisting components are hand assembled to the completed main bodies [Fig. 9(4)]. The twisting components were sized to vary the amount of deflection during assembly (Table I), and there were dies with both posts (type P) and rings (type R) on the surface of the main body that is directly below the twisting component when assembled (Table II). Thus, an assembly can use any combination of spring geometry, main body surface, and spring tip deflection.

In the design of the process flow, precautions were taken to obtain the straightest possible sidewalls for the twisting component and the springs because the contact between the two components determines the precision of assembly. For this reason, the original process flow used a sputtered aluminum thin film as hard mask for the DRIE step of the top wafer. Unfortunately, photoresist peeled off during the wet etch of the aluminum and underlying protective oxide. Therefore, for the second iteration of the process, a thin film of PECVD oxide was used as hard mask, which gave excellent results. All DRIE steps were followed by a 20-s nonpassivated DRIE etch (SF_6 plasma only) to smooth the sidewalls and thus increase the maximum allowable stress in the silicon structures [22].

Laser-cut twisting components were also fabricated using 500-μm-thick polyimide wafers and were used with silicon main bodies to explore the electrical performance of the in-plane assembly method (see Section IV-D) and demonstrate the versatility of the assembly method.

IV. MECHANICAL AND ELECTRICAL CHARACTERIZATION OF THE ASSEMBLY

A total of 36 devices were built, assembled, and characterized. Half of the devices used an aluminum film to etch the springs, while the rest used an oxide film for the same purpose. Metrology was conducted to determine the misalignment and repeatability of the assembly method. Also, electrical tests were performed to characterize the leakage current and the maximum allowable bias voltage of the method. Finally, selected data of a high-voltage MEMS array that uses the in-plane assembly method are provided to demonstrate that the approach works.

A. *Assembly, Disassembly, and Robustness*

A small laser-cut plastic tool was used to assemble the devices. The tool engages a set of holes patterned on the twisting component (Fig. 8) to apply a torque using two fingers and a twisting motion. The torque needed to rotate the electrode into place perceptibly depends on the roughness of the sidewalls, the stiffness of the springs, and how much they are deflected. The positioning of the spring tips into the notches produces an audible click. The whole assembly process usually takes less than 30 s. Once assembled, the twisting component can be disassembled from the main body by prying it up, using a pair of tweezers. For some of the looser fitting electrodes, it is also possible to detach the twisting component by applying a large-enough torque while counter rotating the twisting component. During assembly, the twisting component must be fully rotated until a reaction force substantially larger than the frictional assembly force is experienced. In the initial measurements, a few of the devices had large misalignments (50 μm). Inspection of the device using an optical microscope revealed that the spring tips were not completely in their notches. It also helped to wiggle the twisting component with the assembly tool to make the spring tips fall into their notches and thus reduce the misalignment to levels due to the assembly method only. This problem mainly occurred with the devices that used an aluminum etching mask, perhaps because they had rougher sidewalls.

Overall, the robustness of the springs was found satisfactory. Of the 36 devices that were fabricated (288 springs), three springs broke during fabrication (wafer dismount after DRIE). Only seven devices of the batch that used aluminum as DRIE hard mask were assembled. In this process, a total of four springs broke. All the devices that used silicon oxide as DRIE hard mask were assembled, resulting in one lost spring during the initial assembly. No springs were lost during disassembly or any other manipulation of the devices after the initial assembly. The authors believe that the devices that used an Al film as DRIE hard mask lost more springs than the devices that used a SiO_2 film as DRIE hard mask because the edges of the devices that used Al as DRIE hard mask were substantially rougher. The wet etching of the oxide film beneath the Al film attacked the Al film, resulting in rough edges that were transmitted to the DRIE sidewalls. Higher roughness of the spring edges results in a smaller allowable tensile stress before failure (and, therefore, smaller allowable spring tip deflection) because, in single-crystal silicon, the size of the microcracks determines its mechanical performance [22]. However, the assembly

TABLE III
METROLOGY OF THE ASSEMBLY TEST STRUCTURE FABRICATED USING AN OXIDE FILM AS DRIE HARD MASK

Device	X (μm)	Y (μm)	θ (’)	d_o (μm)	d_M (μm)	Comment
1-A-P-II	-6.3	-1.4	-2	6.5	10.9	
1-B-P-I	-5.7	1.4	-0.3	5.9	6.5	
1-C-P-III	-9.8	-1.4	-2.6	9.9	15.6	
1-A-R-I	4.1	4	0.9	5.7	7.7	
1-B-R-III	7.6	1.2	2.4	7.6	12.9	
1-C-R-II	10.6	3.6	2.8	11.2	17.2	
2-A-P-III	-7.7	-2.3	-0.1	8	8.2	
2-B-P-II	-7.4	1	-0.8	7.5	9.2	
2-C-P-I	-7.2	-1.4	-1.4	7.4	10.4	
2-A-R-II	-0.3	-3.2	0.5	3.2	4.3	
2-B-R-I	4.7	-2.3	1.7	5.3	9	
2-C-R-III	11.7	-4.7	2.2	12.6	17.4	A broken spring
3-A-P-I	-7.9	-3.4	1.4	8.6	11.6	
3-B-P-III	-12	-6.4	-0.3	13.6	14.3	
3-C-P-II	-10.7	-3	2.1	11.1	15.7	
3-A-R-III	7.6	-1.9	0.6	7.8	9.1	
3-B-R-II	-4.2	11.4	3.8	12.1	20.4	
3-C-R-I	10.6	0.3	3	10.6	17.1	Had to wiggle it
Minimum	-12	-6.4	-2.6	3.2	4.3	
Maximum	11.7	11.4	3.8	13.6	20.4	
Average	-1.3	-0.5	0.8	8.6	12.1	
RMS	8.4	4	2	9.3	13.2	
RMS (isometry corrected)	3.8	5	1.7	6.2	9.6	
Standard Deviation 10 reassemblies	1	1.2	0.5	0.6	1.3	

misalignment on devices with broken springs was found equivalent to the assembly misalignment on devices with the full spring set.

B. Assembly Alignment Measurements

Only the devices that used oxide as DRIE hard mask were included in the study because the devices that used Al as DRIE hard mask had very rough sidewalls, thus having substantially less alignment precision and repeatability. All the 18 devices that used silicon oxide as DRIE hard mask were measured. Two of the devices were measured ten times to verify the repeatability of the assembly. An Electronic Vision Group TBM8 front-to-back alignment metrology tool was used to measure the in-plane misalignment by conducting metrology on the set of crosshairs etched on the twisting component and on the back of the main body. The TBM8 instrument has a 0.21-μm measurement error. Both linear and angular alignment errors were measured. Measurement of the vertical misalignment of the assembly was conducted on a few devices using an interferometric microscope. The vertical metrology revealed that the top of the electrode is aligned with the top of the electrode holder to within 5 μm.

When taking multiple measurements of the same device using the TBM8, the misalignment was always the same within 0.42 μm. As it will be seen, this error is an order of magnitude smaller than the accuracy of the assembly method. However, when the assembly misalignment was measured on a device that is successively rotated by 90°, the measurements differed by several micrometers. The difference between the measurements was consistent with a constant offset being added to each measurement, perhaps due to some tilt in the TBM8 stage. This constant offset for the measurements was corrected in the measurements that are provided in Table III. The reported values (Fig. 10) are the misalignment of the center of the assembly in the x-direction (X), the y-direction (Y), the biaxial misalignment (d_o), the angular misalignment (θ), and the maximum misalignment across the central region of the twisting component—which has a radius equal to 7.5 mm $(d_M = d_o + r|\theta|)$. Because the twisting component is held in position by spring tips at its periphery, it is expected that θ would decrease if the size of the twisting component is increased, while d_o, X, and Y would remain unchanged. In Table III, the device name indicates the wafer number (1, 2, or 3), twisting component type (A, B, or C; see Table I), interface surface type (R or P; see Table II), and spring type (I, II, or III; see Table I). For example, 2-C-R-III indicates a device obtained by inserting a type-C twisting component (75 μm of the final spring tip deflection) from wafer stack 2 into a main body from wafer stack 2 with type-III springs and a ring as twisting component-to-main body interface surface.

C. Analysis of Observed Misalignment

The authors believe that a substantial portion of the observed misalignment was introduced by the contact photolithography

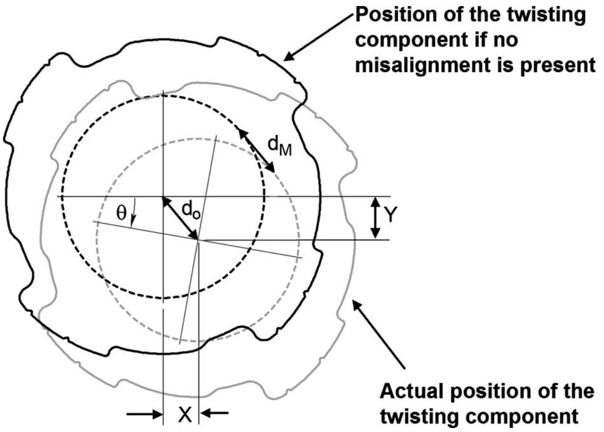

Fig. 10. Variables used to measure the misalignment of the assembly. The misalignment of the center of the twisting component with respect to the center of the main body, i.e., the center of the assembly, was characterized using the center-to-center misalignment in the x-direction X, the center-to-center misalignment in the y-direction Y, the center-to-center biaxial misalignment d_o, the angular misalignment θ, and d_M, i.e., the maximum misalignment across a central region in the twisting component with a radius equal to 7.5 mm.

steps and in the wafer-bonding process. Both sources of misalignment are not directly related to the assembly method but to the particular implementation. Such misalignments could be avoided in a process flow that uses projection photolithography and/or combines on the same mask the features that require precise alignment. Estimates of the error introduced by mask transfer and bonding alignment were conducted to elucidate the misalignment due to the assembly method. In the reported devices, the misalignments due to mask transfer and bonding alignment can be modeled using two isometries (a transformation that preserves distance, i.e., a rigid-body motion). Only rotations and in-plane translations were considered (i.e., 6° of freedom) for each wafer stack. One isometry models the misalignment between the springs and the alignment marks on the main body, while the other isometry models the misalignment between the notches and the alignment marks on the twisting component. Therefore, any misalignment introduced when aligning masks and bonding should be described by these isometries. Each of the six devices in a wafer stack provides three independent measurements (X, Y, and θ), for a total of 18 independent measurements per stack. For each wafer stack, the isometries that minimize the rms deviations were calculated. The difference between the X and Y rms deviations is substantially reduced using the isometry corrections (Table III). In particular, the x-axis values were about twice the y-axis values before the corrections were implemented, although, in principle, they should be about the same because of the symmetry of the test structure. Table III also indicates a correlation between spring tip deflection (given by the electrode type), the interface surface between the twisting component and the main body (R versus P), and the misalignment values in the x-direction. The assembled devices with a type-P interface surface between the twisting component and the main body have lower X values than the devices with a type-R interface surface, while the assembled devices with type-C twisting components, which produce the largest spring tip deflections, have the largest misalignment values in the x-direction. Examining the layout of the devices on the wafer, the authors believe that this observation could largely be explained by a wafer-level rotation in one of the mask alignments. The corrected values result in a biaxial misalignment of 6.2-μm rms and a rotation error of $1.7'$.

The repeatability of the assembly was also characterized. For this purpose, the 3-A-P-I and 1-C-P-III devices were reassembled ten times each. The measurements are shown in Fig. 11, and the standard deviations are in Table III. The assembly/disassembly is repeatable to within a standard deviation of 0.6 μm. This value is an order of magnitude smaller than the 6.2-μm rms obtained after the isometry modeling. Hence, the measured biaxial misalignment cannot be explained by randomness in the assembly process.

The angular misalignment of the assembly may be due to the spring nonidealities. While bending, the springs also deflect axially and rotate. The two added effects could cause a systematic angular offset in the assembled device. The devices with a type-P interface surface between the main body and the twisting component twist opposite to the devices that have a type-R interface surface. Therefore, it is expected that this systematic offset occurs in opposite directions between the two types of devices. This offset cannot be explained by isometries. From Table III, it is observed that the angular misalignment for type-P devices is systematically lower than the angular misalignment for type-R devices, and this deviation is greater for higher spring tip deflections (directly linked to the type of twisting component used). Averaging over similar devices, and after taking into account the isometries previously determined, rotational misalignments equal to $0.5'$, $1.5'$, and $1.6'$ are obtained for type-A, type-B, and type-C twisting components, respectively. This is the right order of magnitude for the systematic angular misalignments that one would expect from spring tip motion nonidealities.

Finally, different over-/underetching between the two sides of a spring tip or the two sides of a notch can produce alignment errors that cannot be explained by isometries. For example, nonuniformities in the plasma could cause microloading, which can be corrected to a certain point by fine-tuning of the DRIE recipe and rotation of the wafer as the DRIE step advances. This type of variation would cause a random deviation in the misalignment measurements but would be consistent when a device is disassembled and reassembled. If this effect contributes to the remaining variation after isometry correction, then we hypothesize that making the spring tip and notch smaller should improve alignment accuracy.

D. Electrical Testing

The in-plane assembly method is intended for high-voltage MEMS arrays. However, the test structure originally has no insulating features. Several insulation strategies were investigated, and all the electrical tests were conducted at atmospheric pressure. The following is a summary of the successful electrical insulation implementations.

1) *Thin-film dielectric coating of the twisting component.* Twisting components covered with a 10-μm-thick

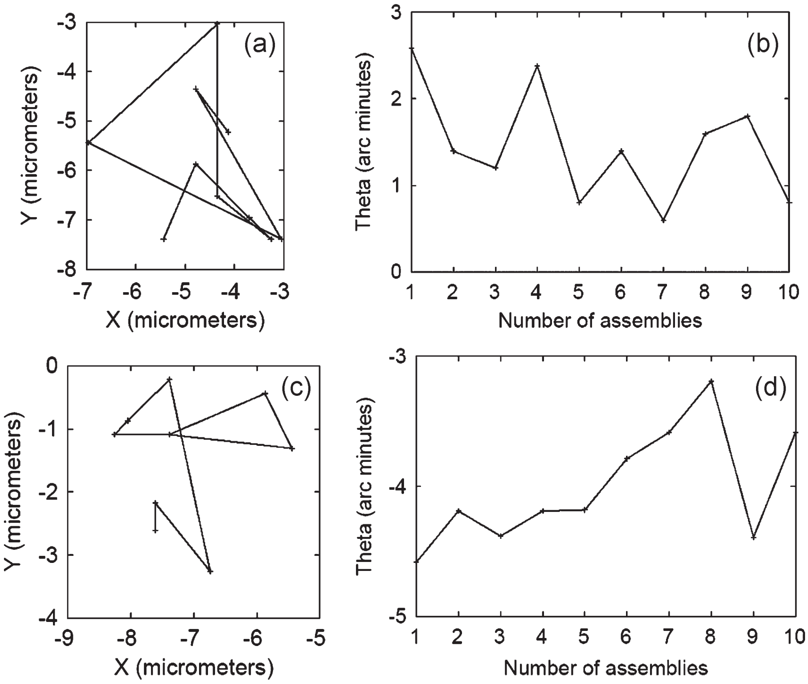

Fig. 11. Alignment data for reassembly experiments using the 3-A-P-I and 1-C-P-III devices: (a) Central misalignment of the 3-A-P-I device, (b) rotation misalignment of the 3-A-P-I device, (c) central misalignment of the 1-C-P-III device, and (d) rotation misalignment of the 1-C-P-III device.

PECVD silicon oxide film were able to withstand up to 5 kV if probed far from the edges. However, near the edges, the breakdown voltage is around 700 V, probably due to the field enhancement from the DRIE sharp corners. As a result, the breakdown voltage of the assembly was limited to 700 V. Also, an 8-μm-thick parylene film was tested as insulation of the twisting component, resulting in a breakdown voltage between 1.5 and 2 kV, with leakages before breakdown in the hundreds-of-nanoampere range.

2) *Twisting component made of a dielectric material.* Laser-cut polyimide (Cirlex) twisting components were tested. The components had a sputtered aluminum thin film to allow the application of a voltage bias. The electrical tests were inconsistent: one device was able to withstand voltages up to 5 kV with less than 200-nA leakage current, while others broke down at voltages as low as 1.5 kV or had μA-level leakage current at 1 kV. After breakdown, the Al film was often damaged and divided into nonconnected regions.

3) *Insulating substrate bonded to the in-plane assembly structure.* The bottom wafer of the main structure was bonded to a patterned Pyrex wafer, and a trench that was 1–4 mm wide was cut through the silicon so that the central region would be insulated from the outer region (Fig. 12). The top wafer of the main body was bonded using low-temperature fusion bonding [30]. These devices were able to withstand up to 5 kV with a leakage of 20 nA (Fig. 13). However, after continuous dc probing for some time, an irreversible modification of the device would take place, leading to higher leakage (1 nA at 2.5 kV). Wider silicon trenches are more immune to degradation than narrower trenches.

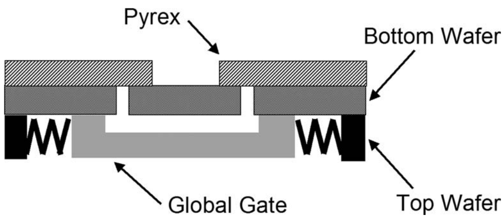

Fig. 12. Schematic of electrical insulation implementation that uses an additional Pyrex wafer bonded to the main body.

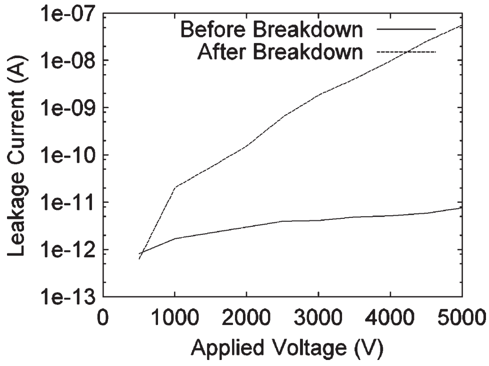

Fig. 13. Typical leakage current versus bias voltage for the device shown in Fig. 12.

E. Selected Data of an Application Example: A Planar Array of Electrospray Emitters

The assembly method has been successfully implemented in a planar array of microfabricated electrospray emitters that is used as ion source for space propulsion applications [31], [32]. The detailed description of this work is beyond the scope of

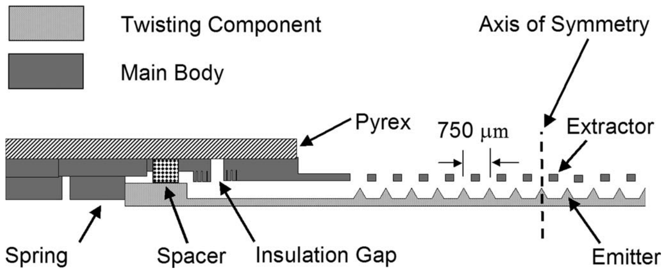

Fig. 14. Cross section of a gated planar array of electrospray emitters that implements the reported assembly technology. The twisting component is the electrospray emitter array, while the main body has a slotted extractor grid to gate the electrospray emitters.

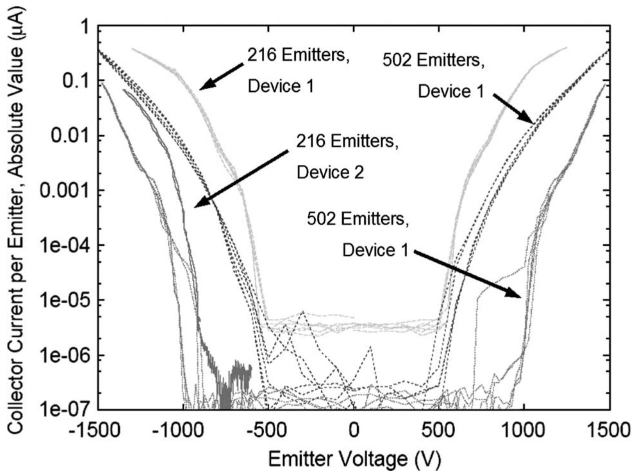

Fig. 15. I–V characteristics of an EMI-BF$_4$ ion MEMS electrospray source that uses the in-plane assembly technology.

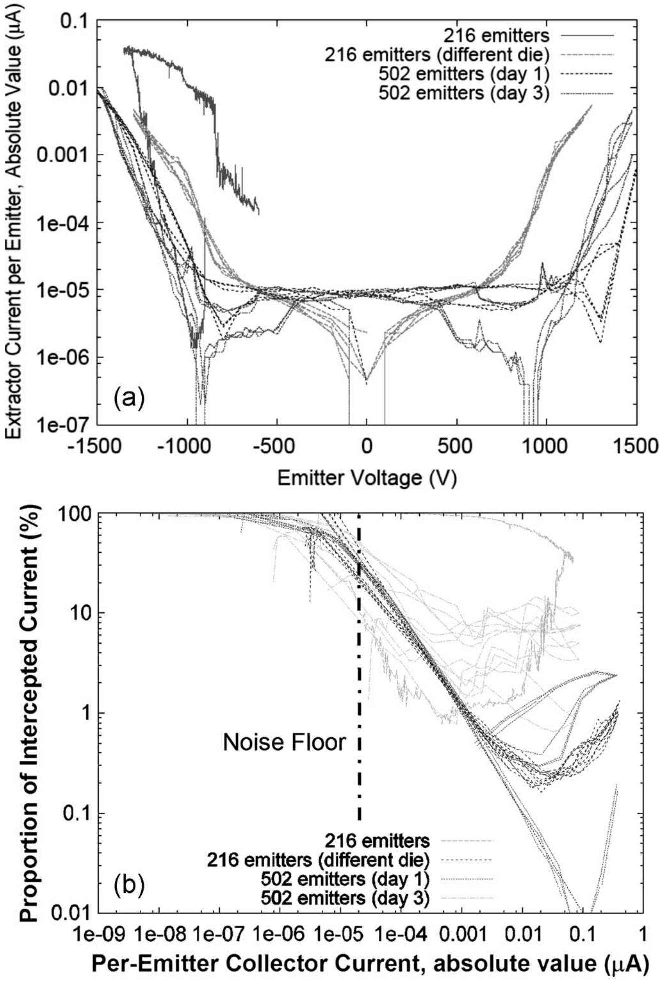

Fig. 16. (a) Gate interception current per emitter versus bias voltage. (b) Normalized gate intercepted current per emitter versus current per emitter.

this paper. A thorough report of the work is provided elsewhere [33]. However, the authors would like to briefly describe the application to provide evidence of the effectiveness of the assembly method. Fig. 14 shows a cross section of the implemented MEMS electrospray ion source. The main body of the device contains the extractor electrode, while the twisting component is the electrospray emitter array. The main component of the electrical insulation system of the electrospray array is the Pyrex layer at the top of the main body. The extractor is a slotted grid with 500-μm apertures and 750-μm pitch. The array is composed of a set of emitting ridges with 750-μm pitch. Each ridge is a linear array of emitters. Each emitter is about 250 μm tall, with 1-μm tip radius, and adjacent emitters part of the same ridge are 275-μm apart. The device has as many as 502 emitters in a 1.13 cm^2 active area, making it the densest and largest working electrospray array with integrated gate reported to date. When assembled, the emitter-to-extractor separation is about 300 μm, which is more than an order of magnitude larger than the assembly precision. A set of four spacers is used to vary the emitter-to-extractor separation without the need to fabricate from scratch new emitter array dies and/or extractor components. The spacers have no effect in the electrical insulation of the MEMS electrospray array, but they influence the start-up voltage of the device and the interception of the electrospray fan by the extractor. The beam divergence of the electrospray sources could be as large as 30° without causing beam interception by the electrode. The gated electrospray arrays were tested in a triode setup, where a voltage bias is applied between the emitter array and the extractor, and the electrospray beam is intercepted by a grounded external collector. Fig. 15 shows the normalized I–V characteristics of the electrospray source when using the ionic liquid EMI-BF$_4$, a propellant that is ideal for deep space propulsion applications because of the high I_{sp} that it can produce [7]. The device has a start-up voltage as low as 500 V, the smallest value reported for an electrospray device. The current per emitter is as large as 0.4 μA, while the noise floor of the experimental setup is less than 0.01 nA. The current per emitter intercepted by the extractor versus extractor voltage is shown in Fig. 16(a), and its value normalized to the collector current per emitter is shown in Fig. 16(b). The noise floor of the intercepted current is about 0.02 nA. The intercepted current is below the noise floor between -750 and 750 V. In Fig. 16(b), it can be seen that once the collector current is higher than the intercepted-current noise level, the intercepted current is less than 10% and, in the majority of cases, below 1%. The low start-up voltages, high emitter density, and low interception current are evidence of the viability of the proposed in-plane assembly method for high-voltage MEMS arrays.

V. CONCLUSION

The design and experimental validation of a hand-actuated in-plane assembly method intended for high-voltage MEMS arrays was presented. In this method, the electrodes and the emitting substrates are assembled using a set of mesoscaled DRIE-patterned springs that lock into small v-shaped notches. The cantilevers are uniformly and azimuthally distributed around the assembly interface to provide low stiffness while the assembly process is in progress and high stiffness once the assembly is completed, which results in a robust assembly. The notches are composed of two 45° planes as a tradeoff between process variation sensitivity and restoring force capability of the assembly. The in-plane assembly method allows the fabrication processes of the device components to be decoupled, particularly enabling substrate optimization of each assembly component. Analysis predicts that the optimal shape for a linearly tapered cantilever implies a cantilever tip height equal to 37% of the cantilever base height, which results in more than a threefold increase in the clamping force for a given cantilever length and deflection, compared to the untapered case. The linear taper profile achieves 80% of the optimal nonlinear taper profile, which would be impractical to fabricate. The assembly method has a biaxial precision of 6.2-μm rms, a rotation precision of $1.7'$, and a repeatability of 0.62 μm. When the sidewalls of the springs are smooth, the structural performance of the springs results in near-100% survivability, even after multiple reassemblies. Metrology of the test structures shows that if one or two springs are missing, the remaining springs are able to assemble the two components without loss in positional accuracy, compared to the case with a full spring set. Experimental results show that it is possible to use a bias voltage as high as 2 kV with leakage currents as small as 1 nA. Selected data of a high-voltage MEMS array application that implements the assembly method were shown as evidence that the assembly method works.

ACKNOWLEDGMENT

This work was conducted using the facilities of the MIT's Microsystems Technology Laboratories (MTL). The authors would like to thank all the MTL staff for their support during the fabrication of the devices.

REFERENCES

[1] M. J. Madou, *Fundamentals of Microfabrication*, 2nd ed. Boca Raton, FL: CRC Press, 2002.

[2] L. F. Velásquez-García and A. I. Akinwande, "A PECVD CNT-based open architecture field ionizer for portable mass spectrometry," in *Proc. 21st IEEE Int. Conf. Microelectromech. Syst.*, Tucson, AZ, Jan. 2008, pp. 742–745.

[3] L. F. Velásquez-García, B. Adeoti, Y. Niu, and A. I. Akinwande, "Uniform high current field emission of electrons from Si and CNF FEAs individually controlled by Si Pillar ungated FETs," in *IEDM Tech. Dig.*, Washington, DC, Dec. 2007, pp. 599–602.

[4] C.-Y. Hong and A. I. Akinwande, "Temporal and spatial current stability of smart field emission arrays," *IEEE Trans. Electron Devices*, vol. 52, no. 10, pp. 2323–2328, Oct. 2005.

[5] G. I. Taylor, "Disintegration of water drops in an electric field," *Proc. R. Soc. Lond. A, Math. Phys. Sci.*, vol. 280, no. 1382, pp. 383–397, Jul. 1964.

[6] L. F. Velásquez-García, A. I. Akinwande, and M. Martínez-Sánchez, "A micro-fabricated linear array of electrospray emitters for thruster applications," *J. Microelectromech. Syst.*, vol. 15, no. 5, pp. 1260–1271, Oct. 2006.

[7] L. F. Velásquez-García, A. I. Akinwande, and M. Martínez-Sánchez, "A planar array of micro-fabricated electrospray emitters for thruster applications," *J. Microelectromech. Syst.*, vol. 15, no. 5, pp. 1272–1280, Oct. 2006.

[8] W. Deng, J. F. Klemic, X. Li, M. A. Reed, and A. Gomez, "Increase of electrospray throughput using multiplexed microfabricated sources for the scalable generation of monodisperse droplets," *J. Aerosol Sci.*, vol. 37, no. 6, pp. 696–714, Jun. 2006.

[9] J. de la Mora and I. G. Loscertales, "The current emitted by highly conductive Taylor cones," *J. Fluid Mech.*, vol. 260, pp. 155–184, 1994.

[10] Y. M. Shin, M. M. Hohman, M. P. Brenner, and G. C. Rutledge, "Experimental characterization of electrospinning: The electrically forced jet and instabilities," *Polymers*, vol. 42, no. 25, pp. 09 955–09 967, Dec. 2001.

[11] R. Krpoun, M. Raber, and H. R. Shea, "Design and fabrication of an integrated MEMS-based colloid micropropulsion system," presented at the Int. Electric Propulsion Conf., Florence, Italy, 2007, Paper IEPC 2007-099.

[12] L. F. Velásquez-García, A. I. Akinwande, and M. Martínez-Sánchez, "Precision hand assembly of MEMS subsystems using DRIE-patterned deflection spring structures: An example of an out-of-plane substrate assembly," *J. Microelectromech. Syst.*, vol. 16, no. 3, pp. 598–612, Jun. 2007.

[13] P. A. Tres, *Designing plastic parts for assembly*, 5th ed. Cincinnati, OH: Hanser Gardner Publ., 2003, ch. 9.

[14] N. Dechey, J. K. Mills, and W. L. Cheghorn, "Mechanical fastener designs for use in the microassembly of 3D microstructures," presented at the ASME Int. Mech. Eng. Congr. RD&D Expo., Anaheim, CA, Nov. 2004, Paper IMECE 2004-62212.

[15] M. Last, V. Subramaniam, and K. S. J. Pister, "Out of plane motion of assembled microstructures using a single-mask SOI process," in *Proc. 13th IEEE Int. Conf. Solid-State Sens., Actuators Microsyst.*, Jun. 2005, pp. 684–687.

[16] R. Prasad, K.-F. Böhringer, and N. C. MacDonald, "Design, fabrication, and characterization of SCS latching snap fasteners for micro assembly," in *Proc. ASME IMECE*, San Francisco, CA, Nov. 1995.

[17] H. Han, L. E. Weiss, and M. L. Reed, "Micromechanical velcro," *J. Microelectromech. Syst.*, vol. 1, no. 1, pp. 37–43, Mar. 1992.

[18] H. Hedler and B. Vasquez, "Self-adhering chip," U.S. Patent 6 756 540, Jun. 29, 2004.

[19] R. M. Bostock, J. D. Collier, R.-J. E. Jansen, R. Jones, D. F. Moore, and J. E. Townsend, "Silicon nitride microclips for the kinematic location of optic fibres in silicon V-shaped grooves," *J. Micromech. Microeng.*, vol. 8, no. 4, pp. 343–360, Dec. 1998.

[20] S. Senturia, *Microsystem Design*. New York: Springer-Verlag, 2000.

[21] V. Kaajakari, *Silicon as Anisotropic Mechanical Material—A Tutorial*. [Online]. Available: http://www.kaajakari.net/~ville/research/tutorials/elasticity_tutorial.pdf

[22] K. Chen, A. Ayon, and S. M. Spearing, "Controlling and testing the fracture strength of silicon on the mesoscale," *J. Amer. Ceram. Soc.*, vol. 83, no. 6, pp. 1476–1484, 2000.

[23] S. Timoshenko, *Mechanics of Materials*, 2nd ed. Boston, MA: PWS-Kent, 1984.

[24] W. C. Young, R. G. Budynas, and R. J. Roark, *Roark's Formulas for Stress and Strain*. New York: McGraw-Hill, 2001.

[25] I.-H. Hwang and J.-H. Lee, "Novel measurement system of the friction coefficients for the DRIE sidewalls," in *Proc. 19th IEEE Int. Conf. Microelectromech. Syst.*, Istanbul, Turkey, 2006, pp. 210–213.

[26] C. Doerrer and R. Werthschuetzky, "Simulating push-buttons using a haptic display: Requirements on force resolution and force–displacement curve," in *Proc. EuroHaptics*, Edinburgh, U.K., 2002, pp. 41–46.

[27] K. Shimoga, "A survey of perceptual feedback issues in dextrous telemanipulation: Part I. Finger force feedback," in *Proc. IEEE VRAIS*, Seattle, WA, 1993, pp. 263–270.

[28] R. C. Hibbeler, *Structural Analysis*, 3rd ed. Englewood Cliffs, NJ: Prentice-Hall, 1997, ch. 9–15.

[29] H. V. Jansen, M. J. de Boer, R. Legtenberg, and M. C. Elwenspoek, "The black silicon method: A universal method for determining the parametric setting of a fluorine-based reactive ion etcher in deep silicon trench etching with profile control," *J. Micromech. Microeng.*, vol. 5, no. 2, pp. 115–120, 1995.

[30] A. Weinert, P. Amirfeiz, and S. Bergson, "Plasma assisted room temperature bonding for MST," *Sens. Actuators A, Phys.*, vol. 92, no. 1, pp. 214–222, Aug. 2001.

[31] B. Gassend, L. F. Velásquez-García, A. I. Akinwande, and M. Martínez-Sánchez, "A fully integrated microfabricated externally wetted electrospray thruster," presented at the 43rd AIAA/ASME/SAE/ASEE Joint Propulsion Conf., Cincinnati, OH, Jul. 8–11, 2007, Paper AIAA-2007-5182.

[32] B. Gassend, L. F. Velásquez-García, A. I. Akinwande, and M. Martínez-Sánchez, “Fabrication of a fully-integrated electrospray array with applications to space propulsion,” in *Proc. 21st IEEE Int. Conf. Microelectromech. Syst.*, Tucson, AZ, Jan. 2008, pp. 976–979.

[33] B. Gassend, L. F. Velásquez-García, A. I. Akinwande, and M. Martínez-Sánchez, “A microfabricated planar electrospray array ionic liquid ion source with integrated extractor,” *J. Microelectromech. Syst.,* to be published.

Blaise Gassend was born in Nice, France, in 1978. He received the Diplôme d’Ingénieur degree from the Ecole Polytechnique, Palaiseau, France, in 2001, and the M.S. degree in physical random functions and the Ph.D. degree in microfabricated electrospray thruster arrays from the Department of Electrical Engineering and Computer Science, Massachusetts Institute of Technology, Cambridge, in 2003 and 2007, respectively.

He is currently an Associate in the Electrical and Semiconductor Practice with Exponent, Inc., Menlo Park, CA, where he consults on failure analysis and litigation support.

Luis Fernando Velásquez-García received the Mechanical Engineer degree (valedictorian of the School of Engineering, *magna cum laude*) and the Civil Engineer degree (valedictorian of the School of Engineering, *magna cum laude*) from the Universidad de Los Andes, Bogotá, Colombia, in 1998 and 1999, respectively, and the M.S. degree in aeronautics and astronautics and the Ph.D. degree in space propulsion from the Massachusetts Institute of Technology (MIT), Cambridge, in 2001 and 2004, respectively.

In 2004, after completing his studies, he became a Postdoctoral Associate with the Microsystems Technology Laboratories, MIT, where he has been a Research Scientist since 2005. He is an expert in micro- and nanofabrication technologies, and his research focuses on the application of micro- and nanofabrication technologies to propulsion, analytical, and power systems. He has conducted research in micro- and nanotechnologies applied to electrospray arrays, carbon-nanotube-based devices, 3-D packaging, mass spectrometry, propulsion, and chemical reactors.

Dr. Velásquez-García is a member of Sigma Xi.

Akintunde Ibitayo (Tayo) Akinwande (S’81–M’86–SM’04–F’08) received the B.Sc. degree in electrical and electronic engineering from the University of Ife, Ife, Nigeria, in 1978, and the M.S. and Ph.D. degrees in electrical engineering from Stanford University, Stanford, CA, in 1981 and 1986, respectively.

In 1986, he joined Honeywell International, Inc., Morristown, NJ, where he initially conducted research on GaAs complementary FET technology for very-high-speed and low-power signal processing. He was later with the Si Microstructures Group, where he conducted research on pressure sensors, accelerometers, and thin-film field emission and display devices. He joined the MIT’s Microsystems Technology Laboratories, MTL, in January 1995, where his research focuses on microfabrication and electronic devices, with particular emphasis on smart sensors and actuators, intelligent displays, large area electronics (macroelectronics), field emission and field ionization devices, mass spectrometry, and electric propulsion. He was a Visiting Professor with the Department of Engineering and an Overseas Fellow with Churchill College, Cambridge University, Cambridge, U.K., in 2002 and 2003. He is currently a Professor with the Department of Electrical Engineering and Computer Science, Massachusetts Institute of Technology, Cambridge. He has authored more than 100 journal publications and is the holder of numerous patents in MEMS, electronics on flexible substrates, and display technologies.

Prof. Akinwande was the recipient of a 1996 National Science Foundation CAREER Award. He is currently a member of the IEEE Nanotechnology Council. He has served on a number of technical program committees for various conferences, including the Device Research Conference, the International Electron Devices Meeting, the International Solid-State Circuits Conference, the International Display Research Conference, and the International Vacuum Microelectronics Conference.